Dual-Band Coherent Perfect Absorption/Thermal Emission From Ultrathin Bilayers

Simin Feng

Michelson Lab, Physics Division,
Naval Air Warfare Center, China Lake, California, USA
*corresponding author, E-mail: simin.feng@navy.mil

Abstract

Dual-band perfect absorption/thermal emission is shown to be a general property of an ultrathin bilayer consisting of a dielectric and a totally reflective layer if the permittivity of the dielectric can be described by Drude-Lorentz (DL) model. The two bands coexist and reside on opposite sides of the Lorentzian resonant frequency where the material loss is small. However, the perfect absorption mechanism for the two bands is distinguishably different. One band is related to Fabry-Pérot phenomenon and the surge of refractive index near the Lorentzian resonance. This band is polarization insensitive. The other band is associated with excitation of Brewster-type mode at the ϵ-near-zero (ENZ) wavelength and occurs only for p-polarized wave at oblique incidences. This mode has a fast-wave non-radiative character and propagates along the ultrathin ENZ layer superimposed on the highly reflective surface. Both bands exhibit wide-angle high emission with a small shift in their center frequencies which can be tuned by tuning the Lorentzian resonance. The resonance-enhanced dual band absorption occurs in the ultrathin DL layer at the weakly absorbing wavelengths as a consequence of an interaction between the total transmission and the total reflection. We demonstrate this phenomenon in a silicon carbide/copper bilayer. The suggested structure may have applications in biological and chemical sensors, IR sensors, thermal emission controls, thermophotovoltaics, and photodetectors.

1. Introduction

There has been considerable interest in various absorbers and thermal emitters due to high demand applications in thermal sensing and energy harvesting. Thermal emission is often characterized by broadband, incoherent, and quasi-isotropic due to the intrinsic random nature of thermal fluctuations. For renewable energy application, it is desirable to have a narrow-band radiation that matches with electronic transition of photovoltaic cells [1] to maximize energy conversion efficiency. In the past few years, photonic bandgap materials have been investigated for changing absorption spectrum and reducing radiation bandwidth [1]–[5]. On the other hand, the ability of controlling emission spectrum and direction also has important applications such as tailoring radiation [6, 7] and thermal sensing. To increase coherence and modify emission characteristics, there has been increasing attention on patterning surface microstructures, such as subwavelength gratings [8]–[11], microcavities [12]–[15], and metamaterials [16]–[19]. It is of great interest in manipulating light to achieve total absorption at a subwavelength scale. Dual-band absorption [20]–[23] is a desired feature for infrared sensors, thermal emitters, and integrated multifunctional devices. In this paper, we will show that dual-band wide-angle perfect absorption is a general property of ultrathin bilayers composed of a primary dielectric layer and a secondary reflective layer if the permittivity of the dielectric can be described by Drude-Lorentz (DL) model. Coherent enhanced absorption is resulted from an interplay between the total transmission of the primary layer and the total reflection of the secondary layer. In the following, we will analyze this phenomenon with both real metal substrate and perfect electric conducting (PEC) ground and demonstrate this property in a silicon carbide (SiC)/copper (Cu) bilayer structure.

2. Coherent perfect absorption

2.1. Basic theory

Figure 1 shows the geometry of the bilayer structure and the coordinate system used in the simulation. Due to the azimuthal symmetry, the polar angle θ is sufficient to describe the direction of the absorption/thermal emission. Consider transverse magnetic (TM) modes, corresponding to non-zero field components H_y, E_x, and E_z. Assume a harmonic time dependence $\exp(-i\omega t)$ for the electromagnetic field. From Maxwell's equations, the magnetic field H_y satisfies the following wave equation:

$$\frac{\partial^2 H_y}{\partial x^2} + \frac{\partial^2 H_y}{\partial z^2} + k_0^2 \epsilon \mu H_y = 0\,, \tag{1}$$

where $k_0 = \omega/c$; the ϵ and μ are, respectively, the permittivity and permeability of the material. Equation (1) permits solutions of the form $\psi(z)\exp(i\beta x)$. Here the transverse wave number β is determined by the incident wave, and is conserved across the interface,

$$\beta^2 = k_0^2 \epsilon \mu - \alpha^2\,, \tag{2}$$

where α is the wave number in the z direction. The functional form of $\psi(z)$ is either a simple exponential $\exp(i\alpha z)$ for the semi-infinite regions or a superposition of $\cos(\alpha z)$

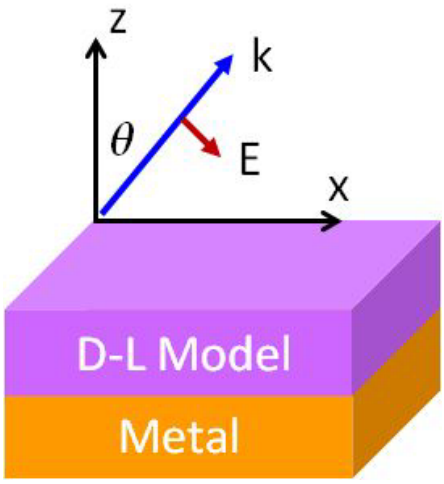

Figure 1: A schematic diagram of a bilayer structure. The permittivity of the primary (top) layer is described by Drude-Lorentz model while the secondary (bottom) layer is highly or totally reflective substrate, such as metal or PEC. The angle θ represents the direction of thermal emission or absorption.

and $\sin(\alpha z)$ terms for the bounded regions along the z direction. The other two components E_x and E_z can be solved from H_y using Maxwell's equations. Only non-magnetic materials are considered. Assume the permittivity of the primary layer in Fig. 1 is described by Drude-Lorentz model, which is given by

$$\epsilon = \epsilon_\infty + \frac{\omega_p^2}{\omega_0^2 - \omega^2 - i\gamma\omega}\,, \tag{3}$$

where the permittivity at the high frequency limit $\epsilon_\infty = 3.8$. The plasma frequency $\omega_p = 0.43\,\mu m^{-1}$; the Lorentzian resonant frequency $\omega_0 = 0.11\,\mu m^{-1}$; and the damping factor $\gamma = 8 \times 10^{-3}\,\mu m^{-1}$. The dispersion in Eq. (3) and the corresponding refractive index are shown in Fig. 2. The Lorentzian resonant wavelength is about $9.1\,\mu$m. For ideal perfect absorption to occur, the substrate should be totally reflective, such as PEC. However, we use copper (Cu) as the highly reflective substrate in our simulation for future potential practical implementation, meanwhile we will use PEC ground to assist our analysis. The complex permittivity of copper can be obtained from Palik [24]. Thus, perfect absorption here is not in a strictly mathematical sense, but rather in a practical sense, meaning close enough to 100%. The complex permittivity of copper and refractive index are provided in Fig. 3 for convenience.

The electromagnetic field can be solved by scattering matrix method and matching boundary conditions at the interface of each layer, i.e. the continuity of H_y and E_x. The transmittance (T) and reflectance (R) of electromagnetic (EM) power can be calculated via the Poynting vector $\boldsymbol{S}$, given by $\boldsymbol{S} = \Re(\boldsymbol{E} \times \boldsymbol{H}^*)$. The fraction of energy absorbed by the structure is described by the absorptance (A), where $A = 1 - T - R$ as required by energy conservation. From the absorption spectrum, the emission spectrum can be obtained from Kirchhoff's law which directly relates the absorptance with the emissivity [25, 26]. For a PEC substrate, there is no transmission and the tangential component of the electric field $E_x = 0$ at the PEC-dielectric interface. Thus, the magnetic field H_y is proportional to the $\cos(\alpha z)$ term if the origin of the z-coordinate is located at the PEC-dielectric interface. By matching boundary conditions at the air-dielectric interface, it is straight forwards to derive the reflection coefficient of the magnetic field as

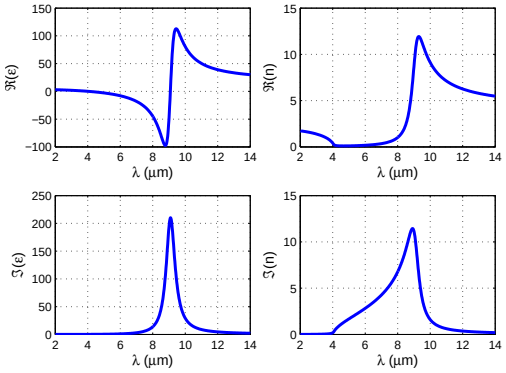

Figure 2: Real (left-top) and imaginary (left-bottom) parts of the permittivity given by Eq. (3), as well as the real (right-top) and imaginary (right-bottom) parts of the corresponding refractive index.

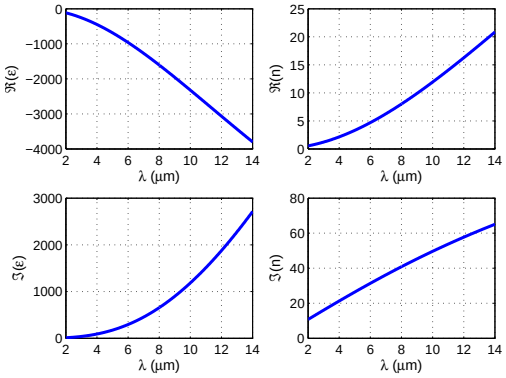

Figure 3: Real (left-top) and imaginary (left-bottom) parts of the permittivity of copper given from Palik [24], as well as the real (right-top) and imaginary (right-bottom) parts of the corresponding refractive index.

$$r = \frac{1 + \eta\tan(\alpha_2 d)}{1 - \eta\tan(\alpha_2 d)}\exp(-i2\alpha_1 d)\,, \tag{4}$$

where the subscripts 1 and 2 refer to, respectively, air and the dielectric. The α_j $(j = 1, 2)$ is given from Eq. (2); and the d is the thickness of the dielectric layer; and

$$\eta = i\frac{\mathcal{Z}_2}{\mathcal{Z}_1} = i\frac{\alpha_2\epsilon_1}{\alpha_1\epsilon_2}\,, \tag{5}$$

where $\mathcal{Z}_1$ and $\mathcal{Z}_1$ are the impedance generalized for oblique incidences; the ϵ_1 and ϵ_2 are, respectively, the permittivity

of air and the dielectric material. The reflected electric field $E_x = \mathcal{Z}_1 H_y$. From the Poynting vector calculation, the reflectance of the power is given by $R = |r|^2$; and thus the absorptance $A = 1 - R$ can be obtained. Perfect absorption occurs when the reflection coefficient is zero where the effective impedance ($\mathcal{Z}_e$) of the ENZ-PEC structure is matched to that of free-space. From Eq. (4), we have

$$\mathcal{Z}_e \equiv -i\mathcal{Z}_2 \tan(\alpha_2 d) = \mathcal{Z}_1 \,. \tag{6}$$

For the real metal substrate, it is an open boundary and the numerical simulation is based on scattering matrix method which computes the transmission and reflection coefficients of the magnetic field (H_y). The associated electric field can be derived from the magnetic field by solving Maxwell's equations. Then, the transmittance (T) and reflectance (R) of the electromagnetic power can be calculated via the Poynting vector. Thus, the absorptance $A = 1 - T - R$.

2.2. Simulation and analysis

In the following discussion and figures, we will use the term "emissivity" and "absorptance" interchangeably for convenience. Figure 4 compares the emission characteristics of the DL/Cu and DL/PEC bilayer structures. The results are very similar using the real metal or PEC as the substrate. Two bright bands with broad emission angle are located on opposite sides of Lorentzian resonance where the material loss is small (see Fig. 2). The angle of perfect emission or absorption depends on the wavelength, dielectric constant, and thickness of the layers. The longer wavelength band around $10 \sim 12\,\mu$m is associated with Fabry-Pérot (FP) resonance and Lorentzian enhanced permittivity and refractive index (see top panels in Fig. 2), which allows the Fabry-Pérot resonant condition to be satisfied for the ultrathin layer. This band has a broader bandwidth and also appears for TE polarized wave; and thus it is insensitive to the polarization as long as the material is isotropic. The shorter wavelength band around $4\,\mu$m is due to the ϵ-near-zero (ENZ) effect [27]-[29] and occurs only for p-polarized waves at non-zero angles of incidence where the normal component of the electric field inside the ENZ medium is extremely high due to the continuity of the normal component of electric displacement field. Since the transmission of the bilayer is zero, perfect absorption occurs at an angle where the reflection of the p-polarized wave is zero, corresponding to excitation of Brewster-type mode [30], which is a fast-wave non-radiative mode propagating along the ultrathin ENZ layer [29]. When the resonant transmissions from the DL layer are totally reflected by the substrate, the coherence-enhanced absorption can occur via multi-reflection and repeated absorption. In the Drude-Lorentz/metal bilayer structures, the shorter wavelength band has a Brewster-type total transmission while the longer band has a Fabry-Pérot type total transmission. The strong coupling between the total transmission of the DL slab and the total reflection of the substrate results in the coherent perfect absorption.

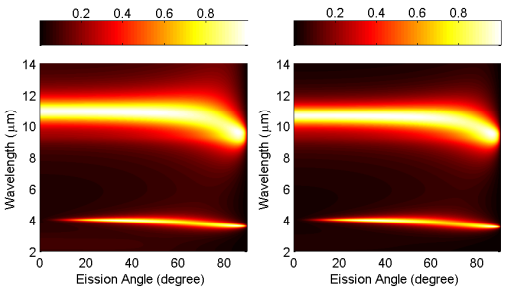

Figure 4: Emissivity of the bilayer in Fig. 1 vs. emission angle (θ) and wavelength. The permittivity of the primary layer is described by Drude-Lorentz model given by Eq. (3). The secondary layer is copper (left) and PEC (right). The thickness of the DL and Cu layers is, respectively, $0.35\,\mu$m and $0.15\,\mu$m. Color bars represent the magnitude of the emissivity. The shorter (longer) wavelength band is located at the left (right) side of the Lorentzian resonance (see left panels in Fig. 2).

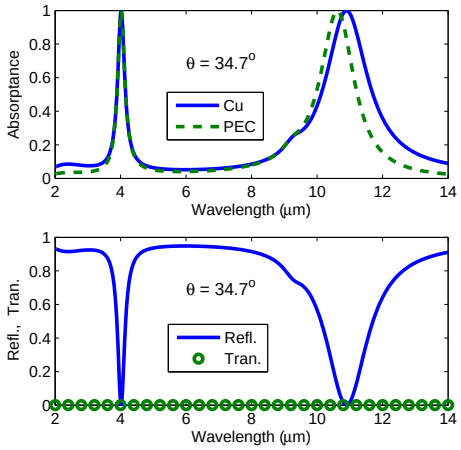

Figure 5: Top panel: absorptance versus wavelength at the perfect absorption angle $\theta = 34.7^\circ$ of the shorter wavelength band when the substrate is Cu (blue-solid) and PEC (green-dashed). Bottom panel: reflectance (blue-solid) and transmittance (green-circles) of the DL/Cu bilayer versus wavelength at the corresponding angle. Simulation parameters are the same as those in Fig. 4.

Interestingly, the large imaginary part of the permittivity at the Lorentzian ENZ wavelength $\lambda \approx 9\,\mu$m does not introduce strong absorption in the ultrathin slab because the huge dissipation destroys the coherence. Thus, at the Lorentzian ENZ wavelength the optical coherence cannot be built-up inside the DL cavity; and the absorption is small due to the ultrathin layer. Absorptance versus wavelength at the perfect absorption angle of the shorter wavelength band is illustrated in the top panel of Fig. 5 for both copper and PEC substrates. The bottom panel of Fig. 5 shows the corresponding transmittance and reflectance for the copper substrate. With the zero transmittance, perfect absorption corresponds to the zero reflection. The spectral and angular locations and bandwidths are related to the permittivity and

material dispersion. With the advance of metamaterial fabrication, the desired spectral locations of peak absorption or emission and other spectral features can be engineered by properly designing the Lorentzian resonant frequency and the damping factor.

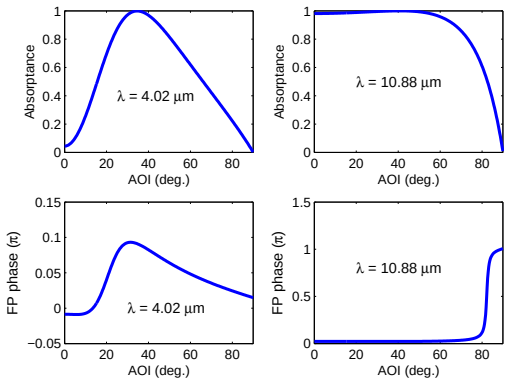

Figure 6: Top panels: absorptance of the DL/Cu bilayer vs. AOI at the perfect absorption wavelength of the shorter band $\lambda = 4.02\,\mu$m (left) and the longer band $\lambda = 10.88\,\mu$m (right). Bottom panels: total round-trip FP phase Φ_F (in the unit of π) vs. AOI at the corresponding wavelength.

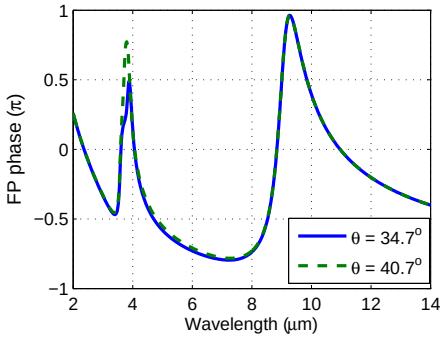

Figure 7: Total round-trip FP phase Φ_F (in the unit of π) vs. wavelength at the perfect absorption angle of the shorter wavelength band ($\theta = 34.7°$, blue-solid) and the longer wavelength band ($\theta = 40.7°$, green-dashed).

The total round-trip Fabry-Pérot phase (Φ_F) of the DL cavity is given by

$$\Phi_F = \phi_1 + \phi_2 + \frac{4\pi d}{\lambda}\Re\left(\sqrt{\epsilon}\right)\cos\theta_d\,, \qquad (7)$$

where the d is the thickness of the DL cavity. The ϕ_1 and ϕ_2 are the reflection phases from the DL medium to air and to the substrate copper, respectively. The third term in Eq. (7) represents the propagation phase inside the DL cavity. The permittivity ϵ is given by Eq. (3). The refraction angle θ_d inside the DL medium is given by

$$\theta_d = \tan^{-1}\left(\frac{\Re(k_x)}{\Re(k_z)}\right) = \tan^{-1}\left(\frac{\beta}{\Re(\alpha)}\right)\,, \qquad (8)$$

where the β is real and determined by the angle of incidence; and α can be obtained from Eq. (2). It is straight forward to calculate the reflection phases ϕ_1 and ϕ_2 from the reflection coefficients at the interface of the two media. In the longer wavelength band in Fig. 4, the blue-shift of the emission frequency as the angle increases can be explained from the cosine factor in Eq. (7). To satisfy the FP resonant condition, as the angle increases, the reduced propagation phase can be compensated by increasing the refractive index (see top-right panel in Fig. 2) through blue-shifting the resonant frequency.

Figure 6 shows the absorptance and the total round-trip Fabry-Pérot phase Φ_F versus angle of incidence (AOI) at the perfect absorption wavelength of the shorter and longer wavelength bands. Figure 7 shows the total FP phase as a function of wavelength at the perfect absorption angle of the shorter and longer wavelength bands. For a single slab, resonant transmission occurs when the total Fabry-Pérot phase is an integer multiple of 2π. As illustrated in Figs. 6 and 7, the near-zero total FP phase at the central wavelength of the longer band is a clear indication of FP resonance-assisted perfect absorption. The shorter band is related to Brewster-induced total transmission and occurs only for p-polarized wave at the oblique incidences (AOI $\neq$ 0). Regardless of different transmission mechanisms, the primary layer forms a resonant cavity whereas the secondary layer provides an optical feedback via reflecting the total transmission from the primary layer, leading to the cavity-enhanced coherent perfect absorption, as a result of the multiple-reflection and repeated absorption.

3. Emission from SiC/Cu bilayer

In this section, we will demonstrate above phenomenon by replacing the ideal Drude-Lorentzian medium with a real material – silicon carbide (SiC). The permittivity of silicon carbide can be obtained from Palik [24]:

$$\epsilon = \epsilon_\infty\left(1 + \frac{\omega_L^2 - \omega_T^2}{\omega_T^2 - \omega^2 - i\gamma\omega}\right)\,, \qquad (9)$$

where $\epsilon_\infty = 6.7$ and the damping factor $\gamma = 4.76\,\mathrm{cm}^{-1}$. The frequency $\omega_L = 969\,\mathrm{cm}^{-1}$ is the longitudinal optical phonon frequency whereas the $\omega_T = 793\,\mathrm{cm}^{-1}$ is the transverse optical phonon frequency. Silicon carbide has a Lorentzian resonance in infrared region as shown in Fig. 8.

The emissivity of the SiC/Cu bilayer as a function of emission angle and wavelength is provided in Fig. 9. A dual-band wide-angle thermal emission from this bilayer structure can be observed. The two coexisting wavelength bands are located on opposite sides of Lorentzian frequency where the material loss is small. Again, there is no strong absorption at the Lorentzian ENZ wavelength ($\sim 12.5\,\mu$m) since the huge dissipation destroys the coherence of the electromagnetic field inside the ultrathin cavity. Thus, the cavity-enhanced absorption cannot be achieved at this wavelength. Due to the smaller damping factor in the Lorentzian resonance of the silicon carbide, the emission bandwidths are narrower than those in above DL model.

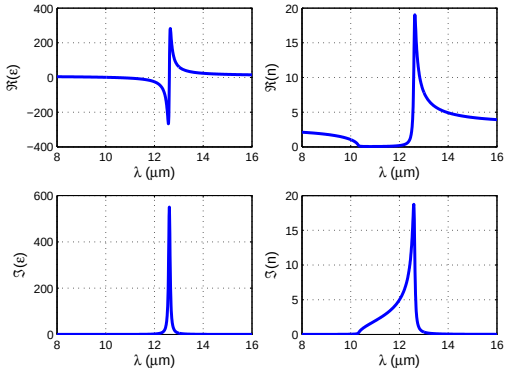

Figure 8: Real (left-top) and imaginary (left-bottom) parts of the permittivity of silicon carbide obtained from Eq. (9), as well as the real (right-top) and imaginary (right-bottom) parts of the corresponding refractive index.

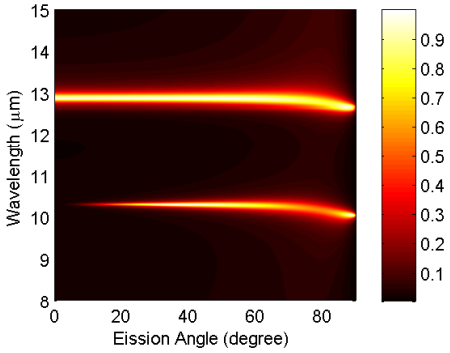

Figure 9: Emissivity of the SiC/Cu bilayer structure vs. emission angle and wavelength. The thickness of the SiC and Cu layer is, respectively, 320 nm and 150 nm. Color bar represents the magnitude of the emissivity. The shorter (longer) wavelength band is located at the left (right) side of Lorentzian resonance (see left panels in Fig. 8).

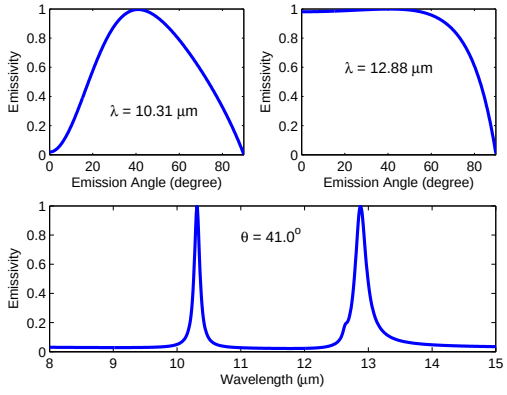

Figure 10: Top panels: emissivity vs. emission angle at the perfect emission wavelength of the shorter wavelength band (left panel, $\lambda = 10.31\,\mu$m) and the longer wavelength band (right panel, $\lambda = 12.88\,\mu$m). Bottom panel: emissivity vs. wavelength at the emission angle $\theta = 41.0°$.

Figure 10 illustrates the emissivity versus emission angle at the perfect emission wavelength of the shorter (top-left) and longer (top-right) bands, as well as the emissivity vs. wavelength (bottom) at the emission angle $\theta = 41°$. The separation between the two bands are less than that in the previous model due to the relatively smaller damping factor in the silicon carbide.

4. Conclusions

In conclusions we have demonstrated the cavity-enhanced dual-band wide-angle absorption/thermal emission around Lorentzian resonance in ultrathin bilayer structures. Many engineered materials can often be effectively described by Drude-Lorentz model, thus the proposed bilayer structures is applicable for a broad range of materials. The layered geometry allows easy integration. The dual-band spectrum and wide acceptance angle are desired features for multi-functional devices including thermal emitters, IR sensors, photodetectors, absorbers, and bolometers.

Acknowledgement

The author gratefully acknowledge NAVAIR's Core Science and Technology Electro-Optics Initiative program.

References

[1] S. Y. Lin, J. Moreno, and J. G. Fleming, Three-dimensional photonic-crystal emitter for thermal photovoltaic power generation, *Appl. Phys. Lett.* 83: 380–382, 2003.

[2] D. L. C. Chan, M. Soljačić, and J. D. Joannopoulos, Thermal emission and design in one-dimensional periodic metallic photonic crystal slabs, *Phys. Rev. E* 74: 016609, 2006.

[3] M. Laroche, R. Carminati, and J.-J. Greffet, Coherent Thermal Antenna Using a Photonic Crystal Slab, *Phys. Rev. Lett.* 96: 123903, 2006.

[4] M. Florescu, K. Busch, and J. P. Dowling, Thermal radiation in photonic crystals, *Phys. Rev. B* 75: 201101(R), 2007.

[5] A. Chutinan and S. John, Light trapping and absorption optimization in certain thin-film photonic crystal architectures, *Phys. Rev. A* 78: 023825, 2008.

[6] A. Alù, M. G. Silveirinha, A. Salandrino, and N. Engheta, Epsilon-near-zero metamaterials and electromagnetic sources: Tailoring the radiation phase pattern, *Phys. Rev. B* 75: 155410, 2007.

[7] K. Halterman, S. Feng, and V. C. Nguyen, Controlled leaky wave radiation from anisotropic epsilon near zero metamaterials, *Phys. Rev. B* 84: 075162, 2011.

[8] J.-J. Greffet, R. Carminati, K. Joulain, J.-P. Mulet, S. Mainguy, and Y. Chen, Coherent emission of light by thermal sources, *Nature* 416: 61–64, 2002.

[9] N. Bonod, G. Tayeb, D. Maystre, S. Enoch, and E. Popov, Total absorption of light by lamellar metallic gratings, *Opt. Express* 16: 15431–15438, 2008.

[10] E. Popov, S. Enoch, and N. Bonod, Absorption of light by extremely shallow metallic gratings: metamaterial behavior, *Opt. Express* 17: 6770–6781, 2009.

[11] J. A. Mason, S. Smith, and D. Wassermana, Strong absorption and selective thermal emission from a mid-infrared metamaterial, *Appl. Phys. Lett.* 98: 241105, 2011.

[12] S. Maruyama, T. Kashiwa, H. Yugamia, and M. Esashi, Thermal radiation from two-dimensionally confined modes in microcavities, *Appl. Phys. Lett.* 79: 1393–1395, 2001.

[13] H. Saia and H. Yugami, Thermophotovoltaic generation with selective radiators based on tungsten surface gratings, *Appl. Phys. Lett.* 85: 3399–3401, 2004.

[14] I. Celanovic, D. Perreault, and J. Kassakian, Resonant-cavity enhanced thermal emission, *Phys. Rev. B* 72: 075127, 2005.

[15] J. R. Brown, A. P. Hibbins, M. J. Lockyear, C. R. Lawrence, and J. R. Sambles, Angle-independent microwave absorption by ultrathin microcavity arrays, *J. Appl. Phys.* 104: 043105, 2008.

[16] Y. Avitzour, Y. A. Urzhumov, and G. Shvets, Wide-angle infrared absorber based on a negative-index plasmonic metamaterial, *Phys. Rev. B* 79: 045131, 2009.

[17] X. Liu, T. Starr, A. F. Starr, and W. J. Padilla, Infrared Spatial and Frequency Selective Metamaterial with Near-Unity Absorbance, *Phys. Rev. Lett.* 104: 207403, 2010.

[18] X. Liu, T. Tyler, T. Starr, A. F. Starr, N. M. Jokerst, and W. J. Padilla, Taming the Blackbody with Infrared Metamaterials as Selective Thermal Emitters, *Phys. Rev. Lett.* 107: 045901, 2011.

[19] L. Li, Y. Yang, and C. Liang, A wide-angle polarization-insensitive ultra-thin metamaterial absorber with three resonant modes, *J. Appl Phys.* 110: 063702, 2011.

[20] Y. Ma, Q. Chen, J. Grant, S. C. Saha, A. Khalid, and D. R. S. Cumming, A terahertz polarization insensitive dual band metamaterial absorber, *Opt. Lett.* 36: 945-947, 2011.

[21] G. Kang, I. Vartiainen, B. Bai, and J. Turunen, Enhanced dual-band infrared absorption in a Fabry-Perot cavity with subwavelength metallic grating, *Opt. Express* 19: 770–778, 2011.

[22] B. Zhang, Y. Zhao, Q. Hao, B. Kiraly, I.-C. Khoo, S. Chen, and T. J. Huang, Polarization-independent dual-band infrared perfect absorber based on a metal-dielectric-metal elliptical nanodisk array, *Opt. Express* 19: 15221–15228, 2011.

[23] P. Ding, E. Liang, G. Cai, W. Hu, C. Fan, and Q. Xue, Dual-band perfect absorption and field enhancement by interaction between localized and propagating surface plasmons in optical metamaterials, *J. Opt.* 13: 075005, 2011.

[24] E. D. Palik, *Handbook of Optical Constants of Solids*, Academic, San Diego, 1998.

[25] J.-J. Greffet and M. Nieto-Vesperinas, Field theory for generalized bidirectional reflectivity: derivation of Helmholtzs reciprocity principle and Kirchhoffs law, *J. Opt. Soc. Am. A* 15: 2735–2744, 1998.

[26] C. Luo, A. Narayanaswamy, G. Chen, and J. D. Joannopoulos, Thermal Radiation from Photonic Crystals: A Direct Calculation, *Phys. Rev. Lett.* 93: 213905, 2004.

[27] Yi Jin, Sanshui Xiao, N. Asger Mortensen, and Sailing He, Arbitrarily thin metamaterial structure for perfect absorption and giant magnification, *Opt. Express* 19: 11114–11119, 2011.

[28] S. Feng, Loss-Induced Omnidirectional Bending to the Normal in ϵ-near-Zero Metamaterials, *Phys. Rev. Lett.* 108: 193904, 2012.

[29] S. Feng and K. Halterman, Perfect absorption in ultra-thin epsilon-near-zero metamaterials induced by fast-wave non-radiative modes, *arXiv:1112.0580v1*.

[30] G. Shkerdin, J. Stiens, and R. Vounckx, "The relationship between reflectivity minima and eigenmodes in multi-layer structures," *J. Opt. A: Pure Appl. Opt.* 5: 386-396, 2003.